The positive effect of water on acetaldehyde oxidation depended on the reaction temperature and MnO$_2$ structure

Zeyu Zhao [a],[1], Ganggang Li [a],[b],[1], Yonggang Sun [a],[b], Na Li [a],[b], Zhongshen Zhang [a],[*], Jie Cheng [a], Chunyan Ma [a],[b],[*], Zhengping Hao [a],[b]

[a] National Engineering Laboratory for VOCs pollution Control Material & Technology, Research Center for Environmental Material and Pollution Control Technology, University of Chinese Academy of Sciences, Beijing 101408, PR China
[b] Key Laboratory of Environmental Nanotechnology and Health Effects, Research Center for Eco-Environmental Sciences, Chinese Academy of Sciences, Beijing 100085, PR China

ARTICLE INFO

ABSTRACT

The effect of H$_2$O on acetaldehyde oxidation was studied and α-, γ-, δ-MnO$_2$ can be affected by the H$_2$O vapor, while β-MnO$_2$ is hardly affected by the H$_2$O vapor during acetaldehyde oxidation. The H$_2$O vapor can facilitate the catalytic oxidation of acetaldehyde at moderate temperatures (ca. 70~100 °C), with a negative effect observed at high temperatures (>100 °C). The stretching mode of the Mn−O−Mn chains in α-, γ-, δ-MnO$_2$ allows the associatively adsorbed water to absorb on the surface prior to acetaldehyde. Afterwards, acetaldehyde can form hydrogen bonds with the associatively adsorbed water molecules, thus, producing the intermediate carboxylic acid species, which are easily degraded to CO$_2$. The negative effect of H$_2$O on the acetaldehyde oxidation at high temperatures is attributed to the difficulty in adsorbing acetaldehyde on MnO$_2$ via hydrogen bonding with the adsorbed H$_2$O. These findings reveal the role of water in the catalytic oxidation of acetaldehyde.

1. Introduction

Acetaldehyde, a typical oxygenated volatile organic compound (VOC), is generated from the biomass combustion as well as during the production of the industrial products. Acetaldehyde is a crucial photochemical intermediate [1,2], and the exposure to acetaldehyde leads to the sick building syndrome and even various cancers [3]. The previous literature studies have employed various process technologies to eliminate acetaldehyde, such as plasma catalysis [4], photocatalytic oxidation [5–7] and adsorption [8], however, these suffer from secondary pollution and incomplete removal. Notably, the thermal catalytic oxidation is recognized as a promising technique for aldehyde abatement owing to its simple equipment and ease of processing.

Among the catalysts used to eliminate VOCs, the Mn-based catalysts have received a significant attention as the effective and economic alternatives. HZSM-5 catalysts loaded with the manganese oxides or Mn−Co bimetal oxides exhibit a remarkable performance in the post-plasma catalysis of acetaldehyde [9]. In a related study, Sun et al. observed that the MnAlO catalyst derived from hydrotalcite exhibited a

strong reducibility and possessed abundant oxygen species, leading to a complete oxidation of acetaldehyde at 140 °C [10]. Moreover, pure MnO$_2$ is widely used in the catalytic oxidation of VOCs due to its excellent reducibility and oxygen mobility [11,12]. In another study, Wang et al. reported that two types of octahedral molecular sieves (OMS-2) could reach the complete conversion of acetaldehyde at 100 and 140 °C [13]. The excellent catalytic activity could be attributed to their weak Mn−O bond and outstanding oxygen mobility. Besides, the MnO$_2$ crystals formed by the combination of the [MnO$_6$] octahedral units have a tunnel or layered structure, which holds the alkali-metal ions or water molecules. Therefore, the structural features of MnO$_2$ result in different catalytic performance during the oxidation reactions [12,14,15].

As an inevitable factor during the exhaust gas treatment, the coexistence of water vapor usually impacts the catalytic activity during the oxidation of VOCs. Typically, the water vapor can compete with formaldehyde or oxygen molecules on the active sites of MnO$_2$ for adsorption, thus, resulting in an inhibition effect on the catalytic activity at 35 °C [16]. However, the water vapor also leads to some positive effects in

---

the MnO_2 catalysts. For instance, the water vapor supplements the consumed surface hydroxyl groups and accelerates the desorption of the carbonate species, which consequently enhances the formaldehyde degradation at room temperature [17,18]. In a related study, Sun et al. reported that the H_2O vapor has a negative effect during the acetone oxidation on MnAlO catalyst at 150 ℃, however, the negative effect disappeared at 190 ℃ [19]. In general, there is a strong correlation between the role of H_2O and temperature during the catalytic reactions. However, the in-depth studies revealing the effects of H_2O on the catalytic oxidation of acetaldehyde are still needed.

Herein, four types of manganese oxide materials with different crystal structures (α-MnO_2, β-MnO_2, γ-MnO_2 and δ-MnO_2) were synthesized, and acetaldehyde was chosen as a typical VOC for studying the catalytic oxidation. Interestingly, a positive effect was triggered by H_2O on the acetaldehyde oxidation reaction in a moderate temperature range, while a negative effect emerged over 100 ℃. The reaction mechanism, especially for explaining the positive effect below 100 ℃, was determined from the amount of the adsorbed H_2O, adsorption state of H_2O and the intermediates formed during the reaction. The findings reported in the study can provide insights about the influence of the water vapor during the oxidation reaction, thus, promoting the development of the water-resistant catalysts.

2. Experimental section

2.1. Catalyst preparation

α-MnO_2, β-MnO_2, γ-MnO_2 [20] and δ-MnO_2 [21] were synthesized by using the hydrothermal method.

2.1.1. α-MnO_2
A mixture of 1.05 g $MnSO_4·H_2O$ and 2.50 g $KMnO_4$ was dissolved in 160 mL ultrapure water, followed by stirring for 30 min to form a uniform solution. Next, the solution was transferred to a hydrothermal reactor with Teflon lining (200 mL). After treatment at 160 ℃ for 12 h, the solution was cooled to room temperature. The collected precipitate was washed by deionized water, dried at 80 ℃ and finally calcined at 300 ℃ for 3 h to obtain α-MnO_2.

2.1.2. β-MnO_2 and γ-MnO_2
3.38 g $MnSO_4·H_2O$ and 4.56 g $(NH_4)_2S_2O_8$ were separately dissolved in 50 mL ultrapure water. Subsequently, the latter solution was slowly dropped in the former solution. After stirring for 30 min, the mixture was transferred to a hydrothermal reactor with Teflon lining (200 mL). After treatment at 140 ℃ for 12 h, the solution was cooled to room temperature. The collected precipitate was washed by deionized water, dried at 80 ℃ and finally calcined at 300 ℃ for 3 h to obtain β-MnO_2.

To synthesize γ-MnO_2, the procedure was similar as β-MnO_2, except that the hydrothermal temperature and time were 90 ℃ and 24 h respectively.

2.1.3. δ-MnO_2
3.16 g $KMnO_4$ was sufficiently dissolved in 140 mL ultrapure water, followed by transferring the solution to a hydrothermal reactor with Teflon lining (200 mL). The contents were treated at 200 ℃ for 12 h. After cooling to room temperature, the collected precipitate was washed by deionized water and dried at 80 ℃. Finally, the product was calcined at 300 ℃ for 3 h to obtain δ-MnO_2.

2.2. Catalyst characterization

The X-ray diffraction (XRD) patterns were obtained on a PANalytical X 'pert PRO powder diffractometer (CuKα, 40 kV, 40 mA) in the scanning range 5–90° at an angular speed of 5 °/min.

Intelligent Gravimetric Analyzer (IGA-002, Hiden) comprising of an analytical balance with a sensitivity of 0.1 μg was used for analyzing the static adsorption of water on the catalysts. The adsorption isotherms were determined by setting the pressure steps (the relative pressure ranges of water vapor) from 0 to 1. Prior to the analysis, the catalysts were pretreated in vacuum at 200 ℃ for 3 h.

The thermogravimetry spectrometry (TG) was used to determine the thermal stability of the catalysts. The samples were purged by using the humid air in a U-tube for 30 min before the TG test. The analysis was performed using a simultaneous thermal analyzer (PerkinElmer STA 8000). The samples (~30 mg) were heated from 40° to 900°C at a rate of 10 °C/min with the samples held under the flowing pure N_2 at a rate of 20 mL/min.

The temperature-programmed desorption of water (H_2O-TPD) was measured by using a temperature programmed desorption apparatus coupled with mass spectrometry. The catalyst (100 mg) was pretreated in a N_2 flow at 300 ℃ for 1 h and was subsequently cooled to room temperature. After absorbing the water vapor for 30 min, the catalyst was swept with a N_2 stream for 30 min. The temperature was increased from 50 to 600 ℃ (10 ℃/min) under N_2 flow, and the desorbed H_2O was detected by a mass spectrometer (Omistar, Pfeiffer).

The $H_2^{18}O$ isotope exchange experiment was performed on a Micromeritics Autochem 2920 chemisorption analyzer connected with a mass spectrometer (HPR-20 R&D, Hiden Analytical). Briefly, 50 mg catalyst was placed in a U-shaped quartz reactor and pretreated at 300 ℃ for 1 h under N_2 flow (50 mL/min). Afterwards, MnO_2 was placed in the reactant flow (500 ppm CH_3CHO and 10.5% O_2/N_2, total flow 50 mL /min) at 120 °C, and the signals ($m/z = 18, 20, 44, 46$) were recorded by mass spectrometry. After the CO_2 signal ($m/z = 44$) in the efflux became stable, 0.5 mL $H_2^{16}O$ or $H_2^{18}O$ vapor was carried to the reactor by He (25 mL/min) in every pulse. The interval between the two contiguous pulses was 5 min

The Raman scattering analysis was performed on a Renishaw inVia laser Raman spectrometer. The exciting radiation was a 785 nm laser with a power of 300 mW, and the Raman spectra were collected using a CCD array detector. Each reported spectrum represented the average of two scans with an exposure time of 100 s each and a resolution of 2 cm^{-1}. The in situ Raman spectra were measured at the desired temperatures by using the mixed reaction gas (25 mL/min 1000 ppm CH_3CHO and 25 mL/min 21% O_2/N_2) in an in situ Raman cell (MR-HP02, Xiamen Tops Equipment Development Co., Ltd.). The 21% O_2/N_2 stream flowed through the ultrapure water under humid conditions. Prior to the CH_3CHO oxidation tests, the samples were pretreated by air purging at 300 ℃ for 1 h, followed by cooling to room temperature.

The in situ diffuse reflectance infrared Fourier transform spectra (In situ DRIFTS) were recorded using a Bruker Tensor II spectrometer, equipped with an MCT detector and a high temperature reaction sample chamber (Praying Mantis, Harrick). Prior to the analysis, the catalyst sample was pretreated under N_2 flow at 300 ℃ for 1 h. The spectrum at the desired temperature was considered as the relative background, and the sample was subsequently cooled to room temperature. The MnO_2 samples were exposed to the reaction gas (25 mL/min 1000 ppm CH_3CHO and 25 mL/min 21% O_2/N_2), and the spectra were recorded after the reaction reached 95 ℃. The time sequence for recording the spectra was 0, 5, 10, 15, 20 and 25 min. For γ-MnO_2, in the adsorption step, 500 ppm acetaldehyde (25 mL/min) and pure N_2 (25 mL/min) were introduced to the chamber. The DRIFT spectra were sequentially recorded by accumulating 100 scans every minute, with a resolution of 4 cm^{-1}. Subsequently, in the reaction step, the 21% O_2/N_2 (25 mL/min) stream was introduced, instead of pure N_2. After stabilization for 10 min, the DRIFT spectra were sequentially recorded at every temperature. The 21% O_2/N_2 stream flowed through the ultrapure water under humid conditions.

2.3. Evaluation of catalyst performance

The catalytic performance was evaluated using a fixed bed reactor with 100 mg catalyst (40–60 mesh). The feed gas (GHSV 18000

mL·g^{-1}·h^{-1}) was composed of 500 ppm acetaldehyde and 10.5% O_2, with the balance N_2. The reactants and products in the gas flow were detected by a gas chromatography apparatus (Agilent 7890B) equipped with a hydrogen flame ionization detector (FID) and a thermal conductivity detector (TCD). Under humid conditions, the water vapor was carried in the O_2/N_2 stream by a bubbling generator at 20 °C. Using the Antoine equation to calculate the saturated vapor pressure of water, the water concentration in the mixed gas was determined to be about 1.2%. The conversion of acetaldehyde was calculated as follows :

The conversion rate of CH_3CHO:

$$X_{CH_3CHO} = \frac{C_{in} - C_{out}}{C_{in}} \times 100\% \qquad (1)$$

C_{in}: input concentration of CH_3CHO;

C_{out}: output concentration of CH_3CHO.

2.4. Quantum chemical calculation

The density functional theory (DFT) calculations of competitive adsorption were applied through the Vienna ab initio simulation package (VASP) [22] with plane wave basis sets and projector-augmented wave (PAW) pseudopotentials [23]. The Generalized Gradient Approximation (GGA) with the Perdew–Burke–Ernzerhof (PBE) functional was used for all the calculations [24]. The Hubbard U corrections (Ueff = U - J) were more studied with U_{eff} = 5.1 eV [25]. Considering the exposure of dominant crystal planes, the {211}, {110}, {311}, and {100} of α-, β-, γ-, and δ-MnO$_2$ were selected as the calculated surface slabs, respectively. The lattice parameter of α-, β-, γ-, and δ-MnO$_2$ bulks were first optimized with the Monkhorst-Pack k-point of 7 × 2 × 2, 7 × 4 × 4, 2 × 7 × 4, and 4 × 7 × 3, respectively. All MnO$_2$ surface were constructed with the vacuum layer of 15 Å. A Monkhorst-Pack k-point 3 × 3 × 1 was used for all surface calculations with the cut-off energy of 400 eV. The structural optimization was conducted using the conjugate-gradient (CG) algorithm, and the force convergence was set to be 0.05 eV·Å^{-1}. Adsorption energy is from the formula:

$$E_{ad} = E_{total} - E_{slab} - E_{molecule} \qquad (2)$$

Which E_{ad} is the binding energy of the adsorbed molecule to the MnO$_2$ slab, E_{total} is the total energy of the adsorption model, E_{slab} is the energy of MnO$_2$ slab, $E_{molecule}$ is the total energy as an isolated molecule of the adsorbed molecule.

3. Results and discussion

3.1. The structure of MnO$_2$ catalysts

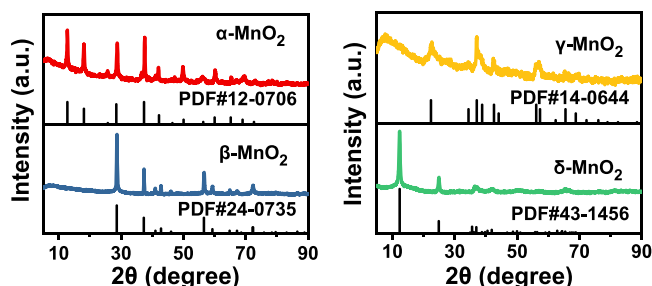The XRD patterns of the MnO$_2$ catalysts are shown in Fig. 1. The as-

Fig. 1. The XRD patterns of α-MnO$_2$, β-MnO$_2$, γ-MnO$_2$ and δ-MnO$_2$.

synthesized α-MnO$_2$, β-MnO$_2$, γ-MnO$_2$ and δ-MnO$_2$ correspond well with the Joint Committee on Powder Diffraction Standards (JCPDS) Powder Diffraction File (PDF) No. 12–0706, 24–0735, 14–0644 and 43–1456, respectively. Thus, the XRD results confirm that α-MnO$_2$, β-MnO$_2$, γ-MnO$_2$ and δ-MnO$_2$ have been successfully synthesized.

FE-SEM was used for investigating the morphology of the prepared MnO$_2$ catalysts. As shown in Fig. S1, α-MnO$_2$ and β-MnO$_2$ are composed of nanorods, with the length ranging from 0.5 to 1 μm. The nanorods in α-MnO$_2$ and β-MnO$_2$ are noted to be mostly randomly stacked. γ-MnO$_2$ presents the dandelion-like spherical clusters with diameters of 4–6 μm. Further, the spherical clusters are assembled by a large number of nanorods. δ-MnO$_2$ displays the clusters made up of petal-like sheets with the interlayer distance of ~50–200 nm, thus, distinguishing it from the other three MnO$_2$ catalysts.

The microstructure of the catalysts was also characterized by Raman spectroscopy. As shown in Fig. S2, the peaks in the range 500–700 cm^{-1} refer to the stretching vibrations of the [MnO$_6$] octahedra [26]. The MnO$_2$ spectra comprise of the basic [MnO$_6$] octahedra with shared edges or vertexes, thus, forming the cross chains and tunnels. Moreover, the location and intensity of the certain peaks can serve as evidence of the tunnels or layers. Specifically, the peaks at 564 cm^{-1} and 635 cm^{-1} in α-MnO$_2$ represent the hollandite structure of the [2 × 2] tunnels [27]. The Raman spectrum of γ-MnO$_2$ is dominated by the main bands at 575 cm^{-1} and 653 cm^{-1}, with several weak peaks at 274, 486, 522 and 753 cm^{-1}. Such Raman features represent the rutile-type structure with the [1 × 1] tunnels as well as the ramsdellite-type structure with the [1 × 2] tunnels, thus, indicating that the [1 × 1] and [1 × 2] tunnels coexist in γ-MnO$_2$ [27,28]. Birnessite δ-MnO$_2$ is noted to possess a two-dimensional layered structure [29]. Obviously, the tunnel and layered structures indicate that the crystal lattice of MnO$_2$ may interact with the molecules or ions of appropriate size (e.g., reactant molecules in the pores, H$_2$O molecules and alkali metal ions between layers, etc.), thus, leading to the complex effects on the catalytic oxidation reactions [12].

The curves of the nitrogen adsorption-desorption isotherms and pore size distribution are illustrated in Fig. S3. Table S1 also presents the specific surface area (S$_{BET}$), pore diameter and pore volume of the MnO$_2$ catalysts. γ-MnO$_2$ possesses the largest specific surface area and pore volume, while β-MnO$_2$ exhibits the minimum area and volume. The order of the specific surface area and pore volume is as follows: γ-MnO$_2$ (59.6 m^2/g, 0.23 cm^3/g) > α-MnO$_2$ (29.9 m^2/g, 0.10 cm^3/g) > δ-MnO$_2$ (21.3 m^2/g, 0.08 cm^3/g) > β-MnO$_2$ (17.8 m^2/g, 0.06 cm^3/g).

The reducibility of MnO$_2$ was surveyed by H$_2$-TPR, as shown in Fig. S4. The reduction peaks in β-MnO$_2$ and γ-MnO$_2$ exhibit a similar profile, comprising of two broad and completely separated peaks at low (290 and 328 °C, respectively) and high (439 and 425 °C, respectively) temperatures. The peak at low temperature can be attributed to the reduction of MnO$_2$ to Mn$_2$O$_3$, whereas the high temperature peak corresponds to the reduction of Mn$_2$O$_3$ to MnO [30]. A broad peak at 346 °C is observed in the α-MnO$_2$ profile, which is attributed to the reduction of MnO$_2$ to Mn$_2$O$_3$. Three reduction peaks, centered at 226, 248 and 329 °C, are observed for δ-MnO$_2$, thus, indicating an enhanced reducibility of δ-MnO$_2$.

3.2. The effect of H$_2$O on catalytic performance

The catalytic performance of the acetaldehyde oxidation reaction over different MnO$_2$ catalysts under dry and humid conditions is shown in Fig. 2. The results show that the CH$_3$CHO conversion and CO$_2$ yield over the MnO$_2$ catalysts increase with the temperature. The complete conversion temperature in the case of α-MnO$_2$ (~120 °C) is observed to be lower than the other three catalysts (~140 °C). For all MnO$_2$ samples, the CH$_3$CHO conversion is higher than the CO$_2$ yield until 100% conversion of CH$_3$CHO to CO$_2$. Considering that CO$_2$ is the final product of the oxidation reaction, the CO$_2$ yield represents an accurate measure of the catalytic performance.
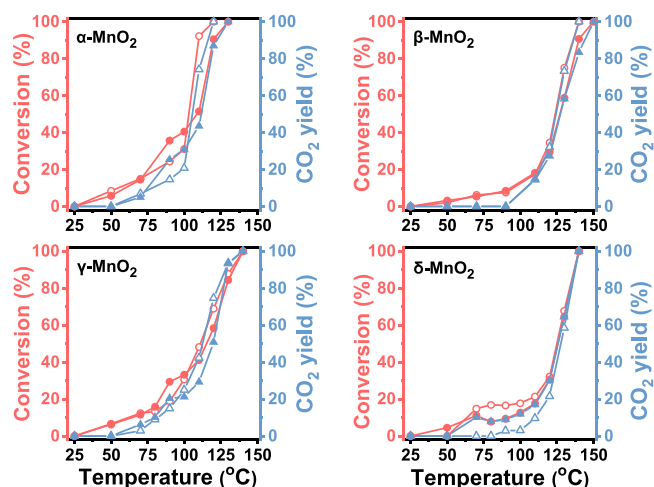
Fig. 2. The catalytic performance of CH$_3$CHO oxidation over α-MnO$_2$, β-MnO$_2$, γ-MnO$_2$ and δ-MnO$_2$ (the hollow and solid points represent the dry and humid condition, respectively; the red and blue lines represent CH$_3$CHO conversion and CO$_2$ yield, respectively).

As reported in the literature studies, the addition of water vapor (1.2 vol%) does not only have a negative effect on the catalytic activity during the acetaldehyde oxidation reaction, although it is generally believed that the competitive adsorption between the H$_2$O molecules and reactants may block the reactive sites [10,31]. However, in a moderate temperature range (70–100 °C), the CO$_2$ yield over α-MnO$_2$ increases under humid conditions as compared with the dry conditions. γ-MnO$_2$ presents a similar phenomenon as α-MnO$_2$, where the moderate range is observed to be 60–90 °C. Particularly, in the case of δ-MnO$_2$, the water vapor hampers the conversion of acetaldehyde, but promotes the CO$_2$ yield almost during the entire reaction process (except at 50 °C). The CO$_2$ yield in the case of α-MnO$_2$ is lowered by adding the water vapor at > 100 °C and < 70 °C. In contrast, β-MnO$_2$ is unaffected by the water vapor before 120 °C, and the CO$_2$ yield only slightly declines after 120 °C. In summary, a moderate temperature allows the water vapor to raise the CO$_2$ yield on α-MnO$_2$, γ-MnO$_2$ and δ-MnO$_2$, while high or low temperatures induce an adverse effect. Among the four MnO$_2$ catalysts, δ-MnO$_2$ presents the most obvious increment, which may be attributed to the structure of MnO$_2$ and needs further investigation.

3.3. Water absorption and desorption behaviors

As depicted in Fig. 3(a, c, e, g), the H$_2$O adsorption/desorption isotherms of MnO$_2$ were obtained by IGA at room temperature. The absolute value of the H$_2$O adsorption exhibits the following order: δ-MnO$_2$ (4.45 mmol/g) > α-MnO$_2$ (3.62 mmol/g) > γ-MnO$_2$ (3.56 mmol/g) > β-MnO$_2$ (0.766 mmol/g). The observed sequence differs from the sequence observed in the case of average pore diameter and pore volume, which indicates that the adsorption amount is not determined solely by the pore-size effect.

Considering the desorption isotherms, the adsorbed H$_2$O amount is not completely desorbed from the MnO$_2$ samples, with δ-MnO$_2$ retaining the largest amount of H$_2$O. The irreversible absorption behavior shows that a large amount of water is chemically adsorbed on the surface. The thermogravimetric analysis (TGA) further revealed the thermal-desorption behavior of water under the programmed-temperature conditions (Fig. 3b, d, f and g). From 100–300 °C, the weight loss can be attributed to the removal of the surface adsorbed water, which is noted to be similar to the amount of adsorbed H$_2$O. In addition, the drops in the curve at > 500 °C are attributed to the loss of the lattice oxygen in the MnO$_2$ crystal. As shown in Fig. S5, the FT-IR analysis also reveals the similar performance. The transmittance signals in the range 3200–3600 cm^{-1} increase significantly after water adsorption on the
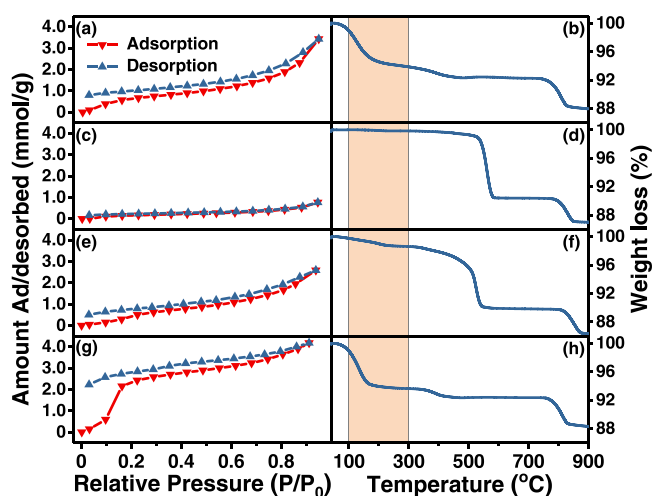

Fig. 3. The H$_2$O-adsorption/desorption isotherms of α-MnO$_2$ (a), β-MnO$_2$ (c), γ-MnO$_2$ (e) and δ-MnO$_2$ (g); and TG curves of α-MnO$_2$ (b), β-MnO$_2$ (d), γ-MnO$_2$ (f) and δ-MnO$_2$ (h).

MnO$_2$ samples. These signals are attributed to the surface hydroxyl groups or chemisorbed water [26]. In brief, the MnO$_2$ samples exhibit different levels of water affinity. Among the different samples, δ-MnO$_2$ and β-MnO$_2$ are the most hydrophilic and hydrophobic manganese oxides.

In order to study the relationship between the adsorption behavior of water and structure of MnO$_2$, the adsorption energy of H$_2$O and CH$_3$CHO on different MnO$_2$ was compared by the density functional theory (DFT)
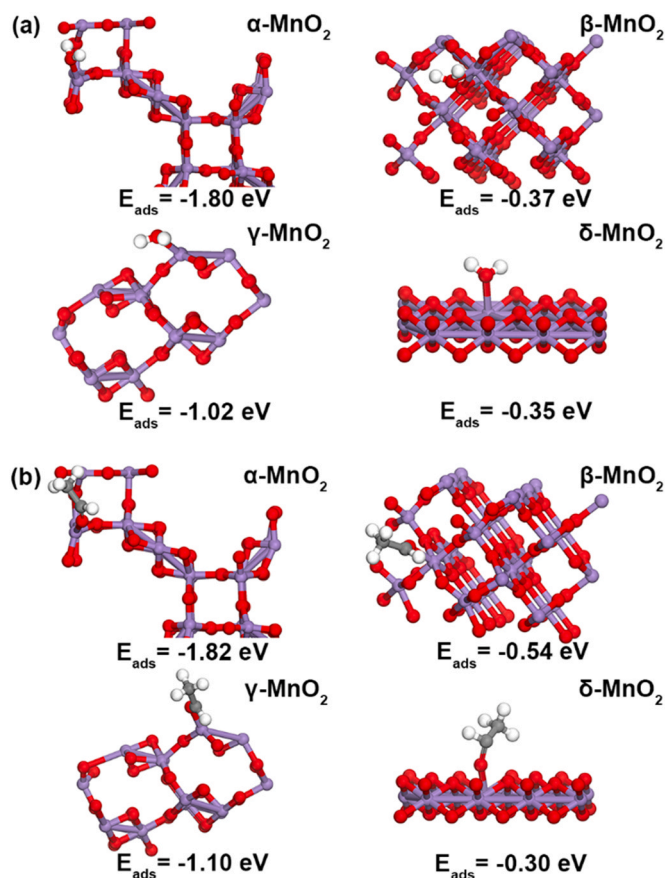

Fig. 4. The adsorption energy of H$_2$O (a) and CH$_3$CHO (b) on α-MnO$_2$, β-MnO$_2$, γ-MnO$_2$ and δ-MnO$_2$.

calculations. As shown in Fig. 4, α-MnO_2 and γ-MnO_2 possess a high H_2O adsorption energy ($E_{ads-H2O}$) (-1.80 eV and -1.02 eV), indicating that the H_2O molecules are more likely to form the chemical bands and get activated on the surface. Both β-MnO_2 and δ-MnO_2 possess a low value of $E_{ads-H2O}$, however, they differ significantly with respect to the amount of the adsorbed water. Furthermore, for α, β and γ-MnO_2, the $E_{ads-H2O}$ value (-1.80 eV, -0.37 eV and -1.02 eV) is lower than the adsorption energy of acetaldehyde ($E_{ads-CH3CHO}$) (-1.82 eV, -0.54 eV and -1.10 eV), thus, representing a weak competitive adsorption between water and acetaldehyde. Conversely, δ-MnO_2 presents a higher $E_{ads-H2O}$ (-0.35 eV) than $E_{ads-CH3CHO}$ (-0.30 eV), thus, signifying a strong competitive adsorption between water and acetaldehyde.

To precisely explore the interaction between the H_2O molecules and MnO_2 surface, the H_2O-TPD-MS analysis was employed. The Gaussian-Lorentz fitting H_2O-TPD curves in Fig. 5 suggest that α-MnO_2 exhibits four desorption peaks at 85, 103, 138 and 279 ℃. On the other hand, β-MnO_2 exhibits four desorption peaks at 86, 130, 290 and 415 ℃, and γ-MnO_2 similarly exhibits four desorption peaks at 84, 111, 158 and 275 ℃. However, δ-MnO_2 exhibits only two desorption peaks at 116 and 142 ℃. As reported in the previous studies [17,32,33], the peaks observed in H_2O-TPD can be attributed to the several different types of water. The temperature of the peak centers in the ascending order follows the sequence: physically adsorbed water in the absence of interaction with the catalyst surface (Peak 1), surface-adsorbed water or water molecules hydrogen bonded to the surface-adsorbed water (Peak 2), "associatively adsorbed" water (Peak 3) and surface hydroxyl groups (Peak 4). Among these, Peak 3 is the most likely case to be active for the acetaldehyde oxidation, for associatively adsorbed H_2O can provide active protons and OH species [32,33]. Consequently, the abundance of the associatively adsorbed water in α-MnO_2 and γ-MnO_2 partially explains the observed acceleration in a certain temperature range. Based on this, the peaks at 116 and 142 ℃ in δ-MnO_2 can be interpreted as Peak 2 and Peak 3, corresponding to its enhanced CO_2 yield under humid conditions. However, the MS signal of β-MnO_2 is evidently inferior as compared to the other MnO_2 materials. In addition, the temperature of Peak 3 reaches 290 ℃, which is much higher than those of the other MnO_2 material, even surpassing the temperature of Peak 4 in α-MnO_2 and γ-MnO_2. Thus, the high desorption temperature of associatively adsorbed water leads to an inconspicuous effect of water on β-MnO_2.

3.4. Mechanism of the role of water

Further analysis to confirm the participation of water vapor on γ-MnO_2 was carried out. To begin with, the $H_2^{18}O$ isotope exchange experiment was conducted. The pulses of $H_2^{16}O$ (Fig. 6a) or $H_2^{18}O$ (Fig. 6b) were introduced every 5 min, after the catalytic oxidation generated a stable CO_2 ($m/z = 44$ and 46) signal. As observed in Fig. 6a, the reactant pulses containing $H_2^{16}O$ merely raise the peak of $C^{16}O_2$, with the negligible fluctuation of $C^{16}O^{18}O$. Instead, as shown in Fig. 6b, a recognizable signal of $C^{16}O^{18}O$ is observed to emerge. The consumption of $H_2^{18}O$ and formation of $C^{16}O^{18}O$ demonstrate that the pathway of the H_2O participation in the acetaldehyde oxidation reaction can be expressed as Eq. 3.

$$CH_3CHO + H_2^{18}O + 2 \cdot 5O_2 \rightarrow CO_2 + C^{16}O^{18}O + 3H_2O \tag{3}$$
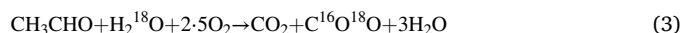
As shown in Fig. 7, the in situ Raman spectra were used to compare the variation in the crystal structure during the reaction under dry and humid conditions. As observed in Fig. S6, all MnO_2 samples are
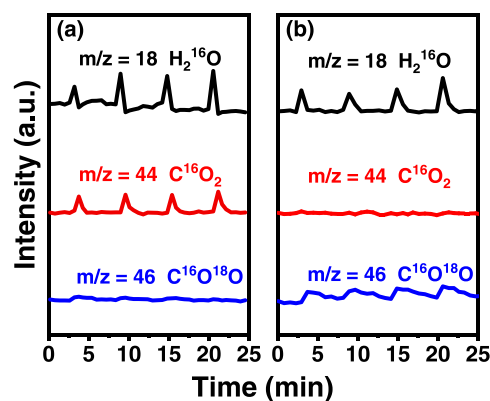

Fig. 6. The $C^{16}O_2$ and $C^{16}O^{18}O$ signals with pulses of $H_2^{16}O$ (a) or $H_2^{18}O$ (b) monitored by MS in the $H_2^{18}O$ isotope exchange experiment.
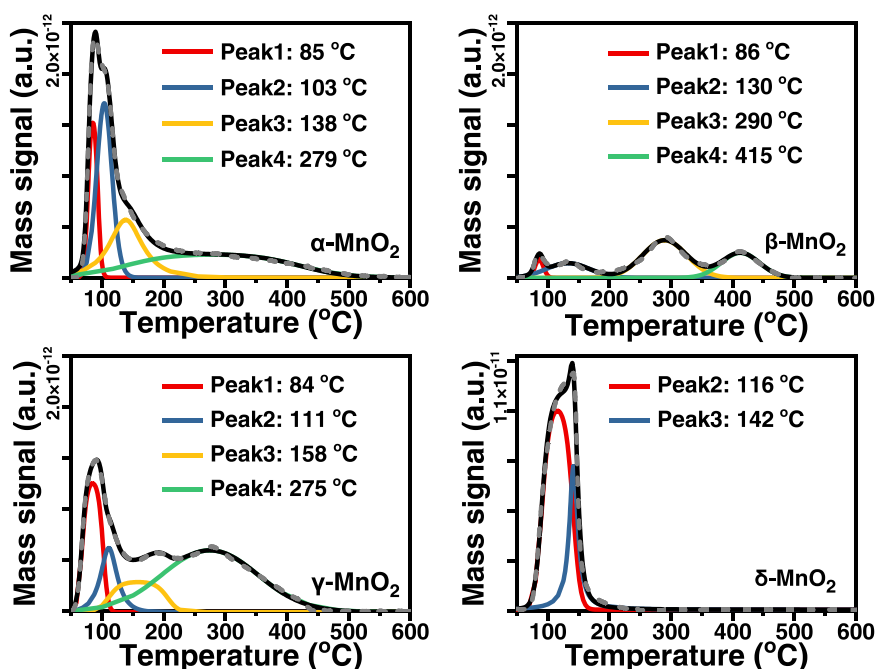
Fig. 5. The H_2O-TPD profiles of α-MnO_2, β-MnO_2, γ-MnO_2 and δ-MnO_2.
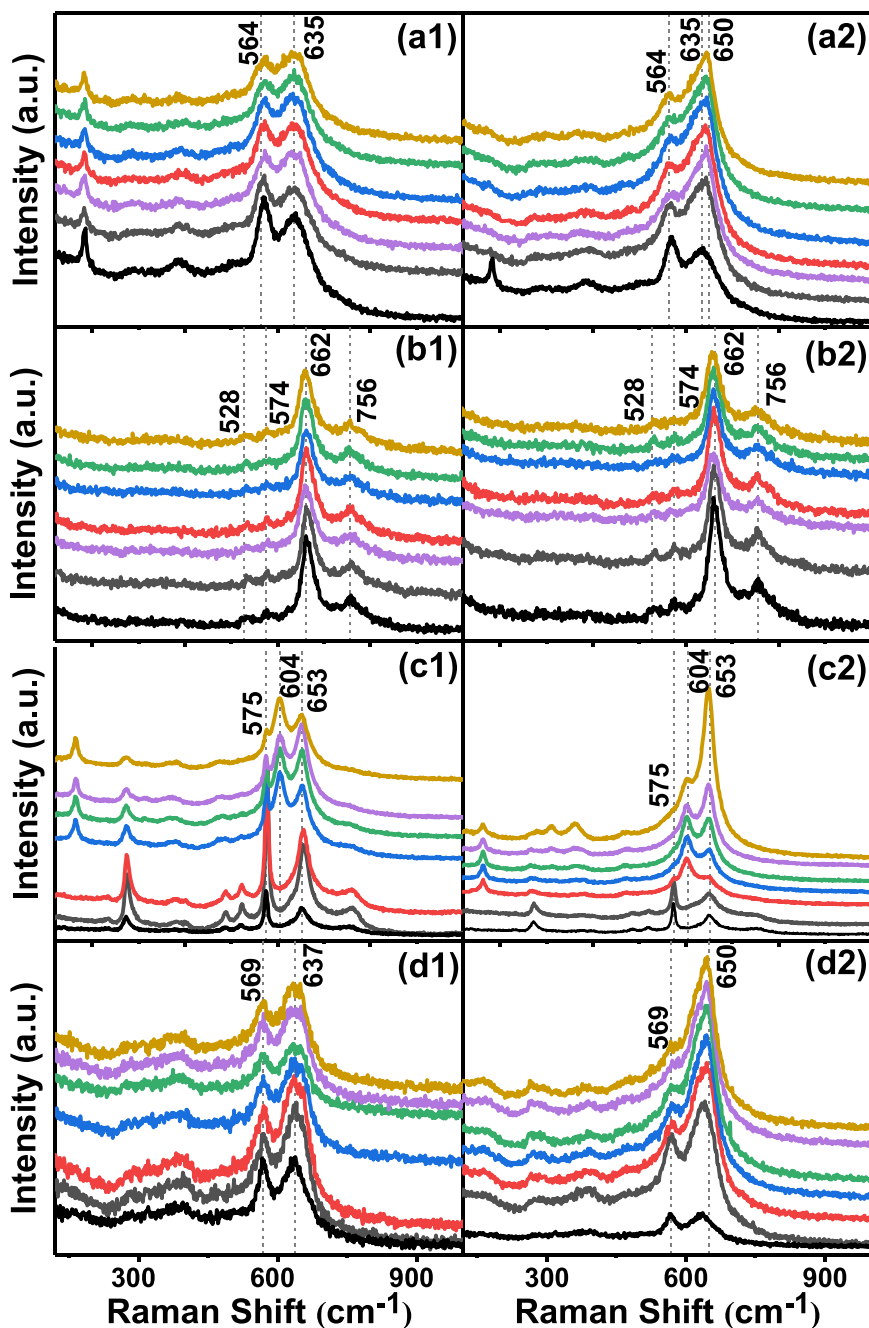
Fig. 7. The in situ Raman spectra of CH_3CHO oxidation on α-MnO_2 (a1) & (a2), β-MnO_2 (b1) & (b2), γ-MnO_2 (c1) & (c2) and δ-MnO_2 (d1) & (d2) under dry (a1, b1, c1, d1) and humid (a2, b2, c2, d2) conditions. The black lines in each subgraph are the spectra of the corresponding MnO_2 recorded in dry air at room temperature. The temperature sequence is from 25 ℃ (grey) to 150 ℃ (brown) i.e., 25 ℃ per line.

thermostable before 200 ℃. In the case of α-MnO_2 in Fig. 7(a1), the main peaks at 564 and 635 cm^{-1} are attributed to the Mn−O−Mn stretching vibrations along the [MnO_6] layer and stretching vibration of Mn−O in the [MnO_6] octahedra, respectively [27,34–36]. An increase in the temperature enhances the activity, which hardly changes the intensities of the two main peaks under dry conditions. However, as shown in Fig. 7(a2), the introduction of the water vapor in the reaction weakens the peak at 564 cm^{-1} on increasing the temperature. Meanwhile, the peak at 635 cm^{-1} is enhanced and blue-shifts to 650 cm^{-1}. In Fig. 7(b1) & (b2), the spectra of β-MnO_2 are unaffected by the water vapor and present the immobile peaks at 574 and 662 cm^{-1}. As shown in Fig. 7 (c1), several obvious changes emerge in the case of γ-MnO_2. It is noticeable that the peaks at 575 cm^{-1} (the stretching modes of the

Mn−O−Mn chains) and 653 cm^{-1} (the Mn−O stretching mode) still dominate in Fig. 7(c1) at low temperatures [26,28,29], whereas the intensity of the peak at 575 cm^{-1} weakens as the temperature is increased, finally reaching a low level. A parallel phenomenon is also observed under humid conditions in Fig. 7(c2), whereas the peak at 575 cm^{-1} almost vanishes at 50 ℃, and a peak at 604 cm^{-1} appears at the same temperature. Meanwhile, the peak at 653 cm^{-1} keeps enhanced on increasing the temperature. For δ-MnO_2 in Fig. 7(d1) & (d2), the main peaks are observed to be located at 569 and 637 cm^{-1}, similar to the main peaks in α-MnO_2 under dry and humid conditions. Specifically, the reaction under dry conditions hardly changes the intensities of the two main peaks, despite increasing the temperature. However, as the catalytic activity improves on increasing the

temperature, the water vapor incorporation weakens the peak at 569 cm^{-1}, and the peak at 635 cm^{-1} simultaneously becomes enlarged and blue-shifts to 650 cm^{-1}. In summary, under humid conditions, α-MnO_2, γ-MnO_2, and δ-MnO_2 present attenuate intensities in the stretching mode of Mn−O−Mn chains and enhanced intensities in the Mn−O stretching mode.

The first main peak located in the range 635–665 cm^{-1} is attributed to the Mn−O stretching mode. This peak is commonly detected in all four types of MnO_2 despite slight differences in the Raman shift. Unlike the other MnO_2 samples, β-MnO_2 lacks the peak around 570 cm^{-1}, which is attributed to the stretching modes of the Mn−O−Mn chains [26,37]. Moreover, β-MnO_2 adsorbs the least amount of water, thus, it is difficult to desorb the associatively adsorbed water from its surface. Hence, it can be speculated that the lack of the stretching modes of the Mn−O−Mn chains is detrimental to the adsorption of the water molecules [36], while the activation and participation of the associatively adsorbed water can interact with the Mn–O–Mn chains and consequently result in the promotion of the catalytic performance.

To explore the effect of H_2O on the reaction mechanism, the in situ DRIFTS analysis of the acetaldehyde oxidation reaction on the MnO_2 catalysts was carried out at 95 °C. As can be observed, the water vapor does facilitate the acetaldehyde oxidation reaction over α-MnO_2, γ-MnO_2 and δ-MnO_2 at 95 ℃, whereas β-MnO_2 is almost inactive for the acetaldehyde oxidation reaction at 95 ℃. As shown in Fig. 8, the peaks at 1717 (α-MnO_2 and δ-MnO_2) and 1730 cm^{-1} (β-MnO_2) can be attributed to the ν(C═O) mode of the adsorbed acetaldehyde [38,39]. The strong signal in the range 1550–1600 cm^{-1} contains two components, namely, ν_{as}(COO) of acetate and formate species. For the acetate species, the ν_{as}(COO) and δ(CH_3) modes are located at 1420–1440 cm^{-1} [16,17, 32], while the ν_{as}(COO) and δ(CH) modes of the formate species emerge at ca. 1350 and 1380 cm^{-1} [40]. Further, the peaks at 1760 and 1630 cm^{-1} are attributed to ν(C═O) in the carboxylate groups and H_2O, respectively [40,41]. The spectra ranging from 2700 to 4000 cm^{-1} (Fig. S7) also confirm the observations, as the stretching vibration of the ν(CH) modes in the carboxylate groups and hydrogen bonded H_2O/hydroxyl lie in the ranges 2800–3000 cm^{-1} and 3200–3600 cm^{-1} [32,42], respectively.

The first step of the acetaldehyde oxidation reaction is the adsorption of acetaldehyde on the MnO_2 surface. Compared with dry conditions, the peak at 1717 cm^{-1} representing the adsorbed acetaldehyde disappears in the case of α-MnO_2 and δ-MnO_2 under humid conditions, as shown in Fig. 8 (a2) and (d2). Thus, the presence of water vapor leads to a competitive adsorption that consequently hinders the direct adsorption of acetaldehyde on the MnO_2 surface. The water molecules adsorb on the MnO_2 surface prior to acetaldehyde, which also corresponds to the findings from the DFT calculations. The adsorption of acetaldehyde on MnO_2 in humid air is attributed to the hydrogen bonding of acetaldehyde with the adsorbed water molecules. As the associatively adsorbed water can provide the active hydroxyls, the water molecules induce a positive effect on the acetaldehyde oxidation reaction over MnO_2. In both dry and humid air, acetate and formate are the typical intermediate species of the acetaldehyde oxidation reaction. The main structure of acetate and formate is -COO (carboxylates), which finally degrades to CO_2 and H_2O [42]. The enhanced intensities in the range 3380–3400 cm^{-1} are attributed to the hydroxyl groups of the intermediate carboxylic acid, which continuously increase on enhancing the reaction duration, particularly under humid conditions (Fig. S7). The whole mechanism has been illustrated in Fig. 9.

Noticeably, γ-MnO_2 presents no obvious peak at 1717 or 1730 cm^{-1} under both dry and humid conditions (Fig. 8(c1) & (c2)). Thus, a DRIFT measurement for the acetaldehyde adsorption on γ-MnO_2 was designed to confirm the reaction mechanism on γ-MnO_2. Initially, acetaldehyde was purged in the cell with N_2 (loading of γ-MnO_2) for 10 min at 25 °C (Fig. S8 (a1) & (a2)). Subsequently, the inlet gas was switched to the reaction gas, and the temperature was raised from 25 to 180 °C, with the recording of the related infrared spectra (Fig. S8 (b1) & (b2)). These
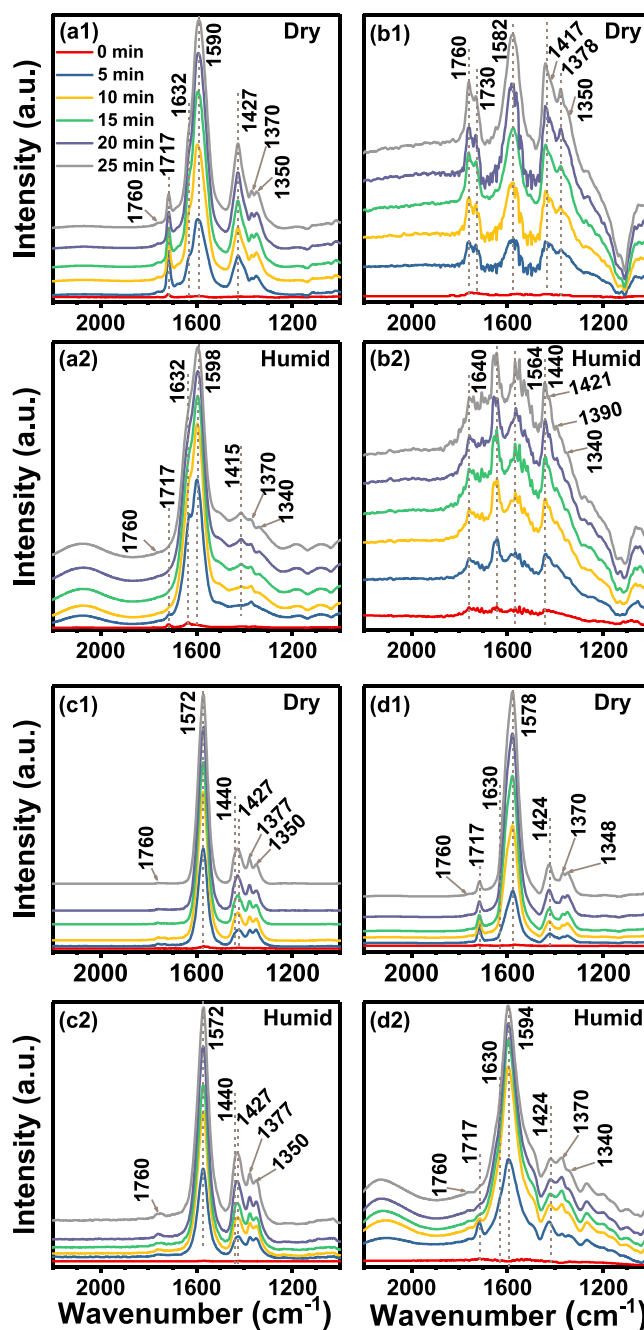

Fig. 8. The in situ DRIFTS spectra of α-MnO_2 (a1) & (a2), β-MnO_2 (b1) & (b2), γ-MnO_2 (c1) & (c2) and δ-MnO_2 (d1) & (d2) under dry (a1, b1, c1, d1) and humid (a2, b2, c2, d2) conditions.

steps were also repeated under humid conditions (Fig. S8 (c1) & (c2) and Fig. S8 (d1) & (d2)). As shown in Fig. S8 (a1), the absorbed acetaldehyde is reflected as a peak at 1700 cm^{-1} under dry condition. Despite no oxygen in the purged air (Fig. S8 (b1) & (b2)), the peaks at 3400, 1760, 1570, 1440, 1421, 1377 and 1350 cm^{-1} are still observed under dry conditions, thus, indicating that the lattice oxygen can oxidize acetaldehyde to acetate and formate intermediate. On introducing the water vapor (Fig. S8 (c1) & (c2)), the H_2O peak at 1635 cm^{-1} is observed to appear, whereas the peak of acetaldehyde at 1700 cm^{-1} disappears. As the reaction gas is loaded with water vapor (Fig. S8 (d1) & (d2)), the intermediate peaks emerge at 1546, 1427 and 1350 cm^{-1}. Therefore, in the adsorption step, acetaldehyde first reacts with the lattice oxygen and produces the mentioned carboxylic acid as intermediates under both
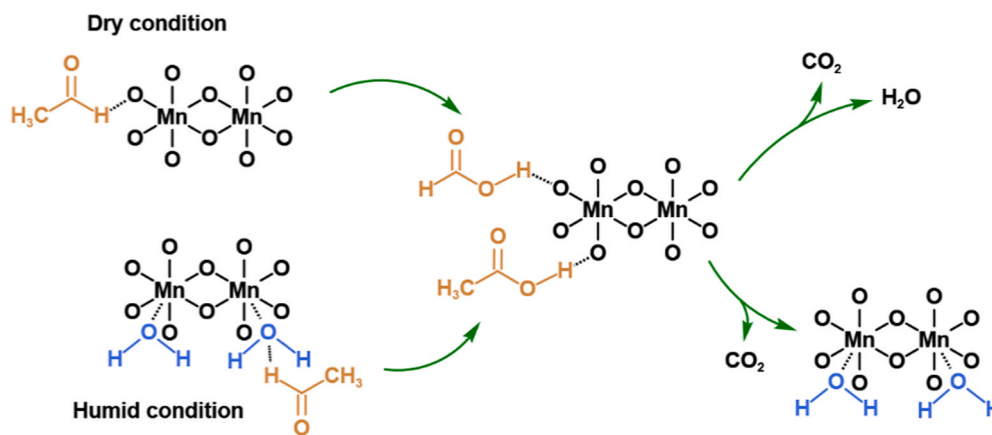
Fig. 9. The mechanism of acetaldehyde oxidation under dry and humid condition.

conditions. Likewise, the water molecules compete with acetaldehyde. Meanwhile this also enables acetaldehyde to make hydrogen bonds with the adsorbed water molecules, and thus, allows the subsequent reactions.

Interestingly, negative peaks appear at ca. 3600 cm^{-1} in Fig S8 (a2) & (b2) & (d2), which originate from the consumption of the related hydroxyl groups. Accordingly, the free hydroxyl groups exhibit the reflection at 3600 cm^{-1} [43], which corresponds to the associatively adsorbed water (H$_2$O-TPD results) in this study. As shown in Fig S8 (c2) & (d2), the water vapor can compensate the consumed associatively absorbed water molecules to some extent [18,42]. Further, the compensation is inhibited after the temperature approaches or reaches the desorption temperature of the associatively adsorbed water.

As the temperature is increased, the hydrogen bonds between water and acetaldehyde cleave gradually. Especially as the temperature surpasses 100 ℃, the water molecules still compete with acetaldehyde without the assistance of the hydrogen bonds. Therefore, the positive effect of the H$_2$O molecules disappears, and the catalytic performance is inhibited.

4. Conclusion

In this study, MnO$_2$ with four different crystal phases has been synthesized for catalyzing the acetaldehyde oxidation reaction, and the impact of water has been specifically examined. The promotion effect distinctly emerges in the case of α-MnO$_2$, γ-MnO$_2$ and δ-MnO$_2$ owing to the stretching of the Mn−O−Mn chains in the MnO$_2$ lattice, which benefits the generation of an abundant amount of the "associatively adsorbed" water. At moderate temperature, the associatively adsorbed water absorbs on the MnO$_2$ surface prior to acetaldehyde. Acetaldehyde can form hydrogen bonds with the associatively adsorbed water, which is probably oxidized by the active hydroxyl groups to form CO$_2$. As β-MnO$_2$ possesses the least extent of the associatively adsorbed water, the water vapor does not promote the acetaldehyde oxidation reaction. In conclusion, the role of water in the catalytic oxidation of acetaldehyde over different MnO$_2$ catalysts has been revealed, thus, enabling the fabrication of the Mn-containing catalysts for acetaldehyde oxidation for organic exhaust gas treatment.

CRediT authorship contribution statement

Zeyu Zhao: Investigation, Formal analysis, Data curation, Validation, Writing – original draft, Ganggang Li: Investigation, Data curation, Validation, Writing – original draft, Yonggang Sun: Methodology, Data curation, Na Li: Methodology, Zhongshen Zhang: Supervision, Writing – review & editing. Jie Cheng: Conceptualization, Funding acquisition, Chunyan Ma: Conceptualization, Supervision, Writing – review &

editing, Zhengping Hao: Conceptualization, Investigation, Supervision, Funding acquisition.

Declaration of Competing Interest

The authors declare that they have no known competing financial interests or personal relationships that could have appeared to influence the work reported in this paper.

Appendix A. Supporting information

Supplementary data associated with this article can be found in the online version at doi:10.1016/j.apcatb.2021.120886.

References

[1] C.T. Yang, G. Miao, Y.H. Pi, Q.B. Xia, J.L. Wu, Z. Li, J. Xiao, Abatement of various types of VOCs by adsorption/catalytic oxidation: a review, Chem. Eng. J. 370 (2019) 1128–1153.

[2] M.S. Kamal, S.A. Razzak, M.M. Hossain, Catalytic oxidation of volatile organic compounds (VOCs) - a review, Atmos. Environ. 140 (2016) 117–134.

[3] C. He, J. Cheng, X. Zhang, M. Douthwaite, S. Pattisson, Z. Hao, Recent advances in the catalytic oxidation of volatile organic compounds: a review based on pollutant sorts and sources, Chem. Rev. 119 (2019) 4471–4568.

[4] Z.X. Jia, M. Ben Amar, D.Z. Yang, O. Brinza, A. Kanaev, X. Duten, A. Vega-Gonzalez, Plasma catalysis application of gold nanoparticles for acetaldehyde decomposition, Chem. Eng. J. 347 (2018) 913–922.

[5] A. Mahmood, X. Wang, X.F. Xie, J. Sun, Atomically dispersed Pt on TiO$_2$ nanosheets for catalytic gaseous acetaldehyde abatement, ACS Appl. Nano Mater. 4 (2021) 3799–3810.

[6] B. Hauchecorne, D. Terrens, S. Verbruggen, J.A. Martens, H. Van Langenhove, K. Demeestere, S. Lenaerts, Elucidating the photocatalytic degradation pathway of acetaldehyde: an FTIR in situ study under atmospheric conditions, Appl. Catal. B: Environ. 106 (2011) 630–638.

[7] Z. Topalian, B.I. Stefanov, C.G. Granqvist, L. Osterlund, Adsorption and photo-oxidation of acetaldehyde on TiO$_2$ and sulfate-modified TiO$_2$: studies by in situ FTIR spectroscopy and micro-kinetic modeling, J. Catal. 307 (2013) 265–274.

[8] J. Jeon, H.I. Kim, J.H. Park, S. Wi, S. Kim, Evaluation of thermal properties and acetaldehyde adsorption performance of sustainable composites using waste wood and biochar, Environ. Res. 196 (2021), 110910.

[9] T. Chang, J.Q. Lu, Z.X. Shen, B. Zhang, Y. Huang, J.J. Cao, H.X. Liu, S.K. P. Veerapandian, N. De Geyter, R. Morent, Post plasma catalysis for the removal of acetaldehyde using Mn-Co/HZSM-5 catalysts, Ind. Eng. Chem. Res. 58 (2019) 14719–14728.

[10] Y. Sun, N. Li, X. Xing, X. Zhang, Z. Zhang, G. Wang, J. Cheng, Z. Hao, Catalytic oxidation performances of typical oxygenated volatile organic compounds (acetone

and acetaldehyde) over MAlO (M = Mn, Co, Ni, Fe) hydrotalcite-derived oxides, Catal. Today 327 (2019) 389–397.

[11] R. Yang, Y. Fan, R. Ye, Y. Tang, X. Cao, Z. Yin, Z. Zeng, MnO_2-Based materials for environmental applications, Adv. Mater. 33 (2021) 2004862.

[12] L. Miao, J.L. Wang, P.Y. Zhang, Review on manganese dioxide for catalytic oxidation of airborne formaldehyde, Appl. Surf. Sci. 466 (2019) 441–453.

[13] R.H. Wang, J.H. Li, Effects of precursor and sulfation on OMS-2 catalyst for oxidation of ethanol and acetaldehyde at low temperatures, Environ. Sci. Technol. 44 (2010) 4282–4287.

[14] T. Chen, H.Y. Dou, X.L. Li, X.F. Tang, J.H. Li, J.M. Hao, Tunnel structure effect of manganese oxides in complete oxidation of formaldehyde, Microporous Mesoporous Mater. 122 (2009) 270–274.

[15] L. Li, M.A. Wahab, H. Li, H. Zhang, J. Deng, X. Zhai, M.K. Masud, M.S.A. Hossain, Pt-modulated $CuMnO_x$ nanosheets as catalysts for toluene oxidation, ACS Appl. Nano Mater. 4 (2021) 6637–6647.

[16] J.L. Wang, J. Li, P.Y. Zhang, G.K. Zhang, Understanding the "seesaw effect" of interlayered K^+ with different structure in manganese oxides for the enhanced formaldehyde oxidation, Appl. Catal. B: Environ. 224 (2018) 863–870.

[17] J. Wang, P. Zhang, J. Li, C. Jiang, R. Yunus, J. Kim, Room-temperature oxidation of formaldehyde by layered manganese oxide: effect of water, Environ. Sci. Technol. 49 (2015) 12372–12379.

[18] Z.Y. Han, C. Wang, X.H. Zou, T.H. Chen, S.W. Dong, Y. Zhao, J.J. Xie, H.B. Liu, Diatomite-supported birnessite-type MnO_2 catalytic oxidation of formaldehyde: preparation, performance and mechanism, Appl. Surf. Sci. 502 (2020), 144201.

[19] Y.G. Sun, X. Zhang, N. Li, X. Xing, H.L. Yang, F.L. Zhang, J. Cheng, Z.S. Zhang, Z. P. Hao, Surface properties enhanced Mn_xAlO oxide catalysts derived from Mn_xAl layered double hydroxides for acetone catalytic oxidation at low temperature, Appl. Catal. B: Environ. 251 (2019) 295–304.

[20] J. Zhang, Y. Li, L. Wang, C. Zhang, H. He, Catalytic oxidation of formaldehyde over manganese oxides with different crystal structures, Catal. Sci. Technol. 5 (2015) 2305–2313.

[21] D. Li, W. Li, Y. Deng, X. Wu, N. Han, Y. Chen, Effective Ti doping of δ-MnO_2 via anion route for highly active catalytic combustion of benzene, J. Phys. Chem. C. 120 (2016) 10275–10282.

[22] G. Kresse, J. Furthmuller, Efficient iterative schemes for ab initio total-energy calculations using a plane-wave basis set, Phys. B: Condens. Matter 54 (1996) 11169–11186.

[23] G. Kresse, D. Joubert, From ultrasoft pseudopotentials to the projector augmented-wave method, Phys. Rev. B 59 (1999) 1758–1775.

[24] J.P. Perdew, K. Burke, M. Ernzerhof, Generalized gradient approximation made simple, Phys. Rev. Lett. 77 (1996) 3865–3868.

[25] D.A. Tompsett, S.C. Parker, P.G. Bruce, M.S. Islam, Nanostructuring of β-MnO_2: the important role of surface to bulk ion migration, Chem. Mater. 25 (2013) 536–541.

[26] S.H. Liang, F.T.G. Bulgan, R.L. Zong, Y.F. Zhu, Effect of phase structure of MnO_2 nanorod catalyst on the activity for CO oxidation, J. Phys. Chem. C 112 (2008) 5307–5315.

[27] T. Gao, H. Fjellvag, P. Norby, A comparison study on Raman scattering properties of alpha- and beta-MnO_2, Anal. Chim. Acta 648 (2009) 235–239.

[28] C. Julien, M. Massot, S. Rangan, M. Lemal, D. Guyomard, Study of structural defects in γ-MnO_2 by Raman spectroscopy, J. Raman Spectrosc. 33 (2002) 223–228.

[29] C.M. Julien, M. Massot, C. Poinsignon, Lattice vibrations of manganese oxides. Part I. Periodic structures, Spectrochim. Acta Part A: Mol. Biomol. Spectrosc. 60 (2004) 689–700.

[30] S. Liang, F. Teng, G. Bulgan, R. Zong, Y. Zhu, Effect of phase structure of MnO_2 nanorod catalyst on the activity for CO oxidation, J. Phys. Chem. C. 112 (2008) 5307–5315.

[31] M.A. Sidheswaran, H. Destaillats, D.P. Sullivan, J. Larsen, W.J. Fisk, Quantitative room-temperature mineralization of airborne formaldehyde using manganese oxide catalysts, Appl. Catal. B: Environ. 107 (2011) 34–41.

[32] C. Ma, C. Yang, B. Wang, C. Chen, F. Wang, X. Yao, M. Song, Effects of H_2O on HCHO and CO oxidation at room-temperature catalyzed by MCo_2O_4 (M=Mn, Ce and Cu) materials, Appl. Catal. B: Environ. 254 (2019) 76–85.

[33] Y. Wang, F. Wang, Q. Song, Q. Xin, S. Xu, J. Xu, Heterogeneous ceria catalyst with water-tolerant Lewis acidic sites for one-pot synthesis of 1,3-diols via Prins condensation and hydrolysis reactions, J. Am. Chem. Soc. 135 (2013) 1506–1515.

[34] G. Zhu, J. Zhu, W. Jiang, Z. Zhang, J. Wang, Y. Zhu, Q. Zhang, Surface oxygen vacancy induced α-MnO_2 nanofiber for highly efficient ozone elimination, Appl. Catal. B: Environ. 209 (2017) 729–737.

[35] T. Gao, M. Glerup, F. Krumeich, R. Nesper, H. Fjellvag, P. Norby, Microstructures and spectroscopic properties of cryptomelane-type manganese dioxide nanofibers, J. Phys. Chem. C 112 (2008) 13134–13140.

[36] C. Ma, S. Sun, H. Lu, Z. Hao, C. Yang, B. Wang, C. Chen, M. Song, Remarkable MnO_2 structure-dependent H_2O promoting effect in HCHO oxidation at room temperature, J. Hazard. Mater. 414 (2021) 125542.

[37] Y.J. Xie, Y.Y. Yu, X.Q. Gong, Y. Guo, Y.L. Guo, Y.Q. Wang, G.Z. Lu, Effect of the crystal plane figure on the catalytic performance of MnO_2 for the total oxidation of propane, CrystEngComm 17 (2015) 3005–3014.

[38] S. Melchers, J. Schneider, A.V. Emeline, D.W. Bahnemann, Effect of H_2O and O_2 on the adsorption and degradation of acetaldehyde on anatase surfaces—an in situ ATR-FTIR study, Catalysts 8 (2018) 417.

[39] R. Kydd, W.Y. Teoh, J. Scott, D. Ferri, R. Amal, Probing surface properties and reaction intermediates during heterogeneous catalytic oxidation of acetaldehyde, ChemCatChem 1 (2009) 286–294.

[40] M. Ma, R. Yang, Z. Jiang, C. Chen, Q. Liu, R. Albilali, C. He, Fabricating $M/Al_2O_3/$cordierite (M = Cr, Mn, Fe, Co, Ni and Cu) monolithic catalysts for ethyl acetate efficient oxidation: unveiling the role of water vapor and reaction mechanism, Fuel 303 (2021) 121244.

[41] X.L. Zeng, B. Li, R.Q. Liu, X. Li, T.L. Zhu, Investigation of promotion effect of Cu doped MnO_2 catalysts on ketone-type VOCs degradation in a one-stage plasma-catalysis system, Chem. Eng. J. 384 (2020), 123362.

[42] C.B. Zhang, F.D. Liu, Y.P. Zhai, H. Ariga, N. Yi, Y.C. Liu, K. Asakura, M. Flytzani-Stephanopoulos, H. He, Alkali-metal-promoted Pt/TiO_2 opens a more efficient pathway to formaldehyde oxidation at ambient temperatures, Angew. Chem. -Int. Ed. 51 (2012) 9628–9632.

[43] C. Hsieh, R.K. Campen, M. Okuno, E.H.G. Backus, Y. Nagata, M. Bonn, Mechanism of vibrational energy dissipation of free OH groups at the air-water interface, Proc. Natl. Acad. Sci. U. S. A. 110 (2013) 18780–18785.